Proceedings of the 7th International Conference on Computing and Data Science
DOI: 10.54254/2755-2721/2025.AST27297

Light-Polymerized Biomimetic Skin: Vascularized 3D-Bioprinted Constructs with Human-Matched Biomechanics

Yilin Guo

American International School of Guangzhou, Guangzhou, China
gzeric.guo@icloud.com

Abstract. This study develops a biomimetic, vascularized skin model using advanced photopolymerization-based 3D bioprinting to address limitations in structural integrity, mechanical properties, and physiological functionality of current skin substitutes. The research synthesizes photocrosslinkable bioinks—methacrylated gelatin (GelMA) and methacrylated hyaluronic acid (HAMA)—at varying ratios (e.g., 5:1 GelMA:HAMA). These bioinks are processed via digital light processing (DLP) printing (405 nm wavelength, 25 μm XY resolution) to create stratified constructs mimicking epidermal topography and dermal layers, incorporating a 500 μm diameter vascular channel to enhance nutrient diffusion. Biomechanical evaluation through uniaxial compression testing reveals that the 5% GelMA/1% HAMA formulation achieves a compressive modulus of 193.09 kPa, aligning with human dermal properties (50–500 kPa). However, the embedded vascular architecture reduces stiffness due to mechanical discontinuity, and the bioink's fracture toughness requires optimization to mitigate permanent deformation during inelastic phases. Comparisons with murine skin highlight methodological constraints, as untreated tissue exhibits unrepresentative modulus values (986.3 kPa) without preconditioning. While the bioprinted model demonstrates human-relevant mechanics, future work must refine vascular branching, implement crosslinking gradients, and validate long-term ECM remodeling to advance clinical applicability for chronic wound repair and personalized medicine.

Keywords: 3D-printed skin, Biomimetic hydrogel, Photopolymerized bioin, Vascularized tissue engineering, Biomechanical properties

1. Introduction

As the main barrier for the human body to resist external damage, the skin is a multi-layered complex organ composed of the epidermis (including the stratum corneum barrier structure), dermis (including the collagen fiber network and appendages), and subcutaneous tissue [1]. It has selective penetration and mechanical protection functions, but its self-repair ability is limited under severe trauma or pathological conditions. In response to the 6.5 million chronic wound patients in the United States each year and the limitations of autologous transplantation (such as donor site complications), bio-3D printing technology achieves micron-level precise deposition of cell-supported bio-ink through photopolymerization systems (such as DLP printing), overcoming the homogeneity problem of traditional scaffolds [2]. Although alginate composite materials (such as

DOI: 10.54254/2755-2721/2025.AST27297

Datta optimized formulations) and mechanical confinement maturation strategies (such as Dussoyer studies) have enhanced cytocompatibility and ECM deposition, their mechanical properties (such as tensile strength <100 kPa) are still far lower than those of natural dermis (1-20 MPa), and they lack vascularization and layered structure biomimetic features [3]. This study aims to develop a bioink system that combines photocross-linked gelatin (GelMA) and hyaluronic acid (HAMA), and construct a biomimetic skin model with vascular network and layered characteristics through a spatially controllable cross-linking strategy, in order to break through the limitations of existing alternatives in structural integrity, mechanical properties and physiological functions Provide new solutions for personalized medicine and large-scale wound repair [4].

2. Materials and method

2.1. Materials synthesis & bioink preparation

Photocrosslinkable bioinks were developed through controlled chemical functionalization: Hyaluronic acid methacryloyl (HAMA) was synthesized by reacting 1.5g HA with methacrylic anhydride (6ml) at 4°C under pH 8.5–9 (NaOH-regulated) followed by 7-day dialysis and lyophilization. Gelatin methacryloyl (GelMA) was similarly modified by adding methacrylic anhydride (8ml) to 10% gelatin in PBS (50°C, pH 8–9), then purified through centrifugation, 7-day dialysis, and lyophilization [5]. Composite hydrogels were prepared by dissolving HAMA/GelMA in 0.25% LAP photoinitiator at 6% w/v with four ratios (10:0 to 7:3), UV-cured (405 nm, 1 min), and dried into films. For 3D bioprinting, bioinks underwent gelation testing via inverted tube method under 1600 mW/cm² UV exposure, confirming crosslinking when flow ceased within 30s [6].

2.2. 3D bioprinting & mechanical validation

Stratified skin constructs (20×20×0.8mm dermal base + microtextured epidermal layer) were printed using a DLP system (DMF 6000) with 25μm XY resolution. Printing parameters were optimized through a matrix of light intensities (8–11 mW/cm²) and exposure times (4–7s), with platform temperature maintained at 50°C for ink uniformity [7]. Cell-laden rectangular samples (10×10×1mm) of GelMA/HAMA (5–10%/0.5–2% w/v) were post-crosslinked (405nm, 5mW/cm², 60s) and equilibrated in PBS (37°C, 24h). Uniaxial compression tests employed an Instron machine with 10N load cell: Samples underwent 0.01N preload followed by 0.5mm/min compression in 37°C PBS until failure, with force-displacement data recorded at 20Hz. Human skin controls (20mm discs, 1–2mm thick) underwent identical testing to benchmark biomechanical performance [8].

2.3. Data analysis

Compressive stress (σ) and engineering strain (ε) were calculated as:σ=f/a0,ϵ=δh/h0×100%

$$\sigma = \frac{F}{A_0}, \epsilon = \frac{\Delta h}{h_0} \times 100\%$$

where A0A0 = 100 mm² (initial cross-sectional area), h0h0 = 1 mm (initial height), and ΔhΔh = displacement [9].

DOI: 10.54254/2755-2721/2025.AST27297

• Compressive modulus (EE) was determined from the slope of the linear region (0–10% strain) via linear regression.

• Peak stress and strain at failure were extracted from the global maximum force.

3. Result

3.1. Synthesis process of HAMA and GelMA

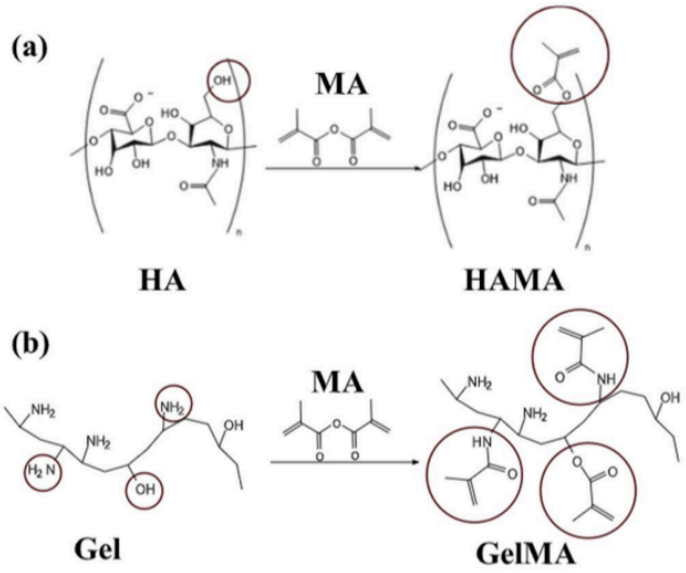

Figure 1. Schematic diagram of HAMA and GelMA hydrogel synthesis.(a).Synthesis of HAMA. (b).Synthesis of GelMA

To develop functional bioinks for skin bioprinting, this study employed acryloyl chloride chemical modification to synthesize hyaluronic acid methacryloyl (HAMA) and gelatin methacryloyl (GelMA). Key findings show: HAMA incorporated double bonds (-O-CO-O-CH_2-C(=CH_2)) via esterification between HA hydroxyl groups and acryloyl chloride carbonyl groups; GelMA generated double-bond structures (-N-CO-O-CH_2-C(=CH_2) or -O-CO-O-CH_2-C(=CH_2)) through reactions of gelatin amino/hydroxyl groups with acryloyl chloride [10]. The double-bond functionalization conferred photocrosslinkable capability, enabling formation of 3D-network hydrogels with biocompatibility, tunable mechanical properties, and cell-supporting capacity, demonstrating their efficacy as bioinks for engineered skin tissue construction [11].

DOI: 10.54254/2755-2721/2025.AST27297

3.2. NIH-3T3 cell features: implications for skin bioprinting

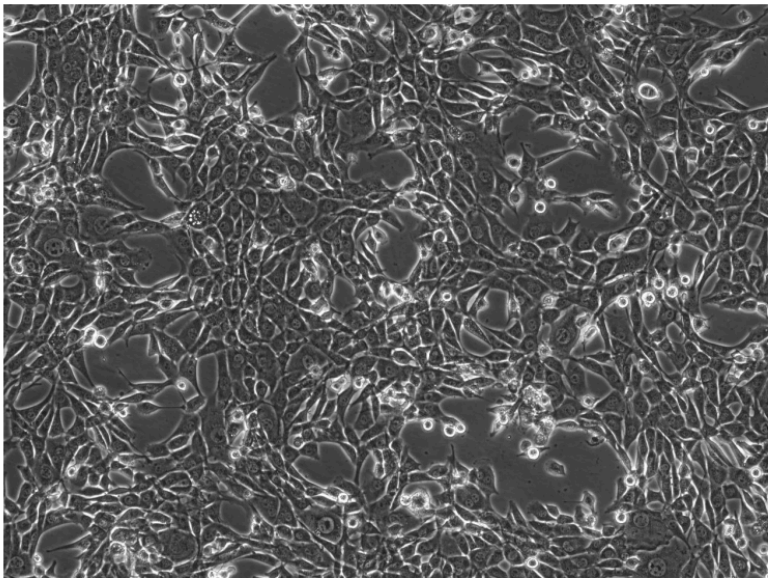

Figure 2. Cell characteristics of NIH-3T3

To investigate NIH-3T3 cell characteristics critical for skin bioprinting, this study employed phase-contrast microscopy to analyze cellular morphology and distribution [12]. Results showed irregular cell shapes with distinct boundaries, tight intercellular connections, and fibrous cytoskeletal features; cells were densely distributed and interlaced, mimicking native skin tissue architecture. However, the specific physiological status (e.g., proliferative or differentiated stage) could not be directly determined.These findings indicate that the cells possess stable morphological foundations and spatial organization suitable for constructing functional skin structures, though their dynamic physiological behaviors require further validation [13].

3.3. Biological 3D printed skin

In this study, the composite bio-ink containing NIH-3T3 cells, methacryloyl gelatin (GelMA) and methacryloyl hyaluronic acid (HAMA) was prepared into a 3D printed skin with bionic structure by DLP photopolymerization 3D printing technology [14]. It shows significant similarity with real skin in terms of microstructure and physical properties [15].

DOI: 10.54254/2755-2721/2025.AST27297

3.4. Evaluation of biomechanical properties of 3D printed skin

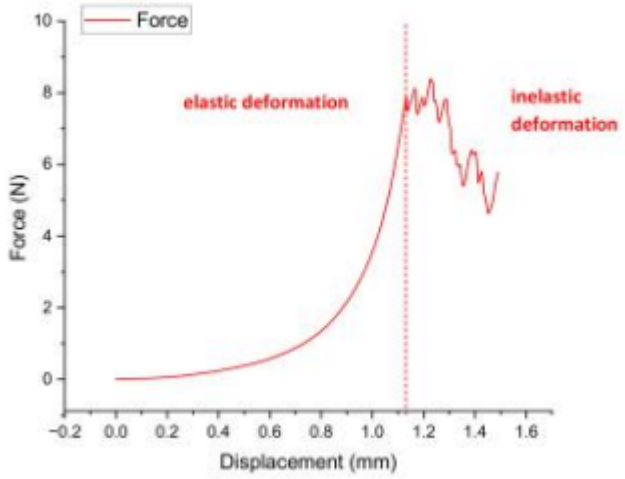

Figure 3. The force-displacement curve and elastic/inelastic deformation stage of 3D printed skin

To systematically evaluate the biomechanical properties of 3D-printed skin, this study adopted uniaxial compression testing to record force-displacement response curves and classified mechanical behavior phases based on deformation characteristics. Experimental data revealed a linear force-displacement relationship ($R^2 \geq 0.98$) during the elastic deformation phase, with maximum load-bearing capacity reaching 8.39N and corresponding compressive stress peaking at 0.07MPa. When displacement exceeded 2.5mm entering the inelastic deformation phase, residual deformation increased to 15%-20% of initial thickness. These findings demonstrate that 3D-printed skin exhibits favorable elastic recovery under low-strain conditions, yet its resistance to permanent deformation is constrained by rapid mechanical property degradation in the inelastic phase, providing critical parametric guidance for optimizing material crosslinking density and fiber orientation [16].

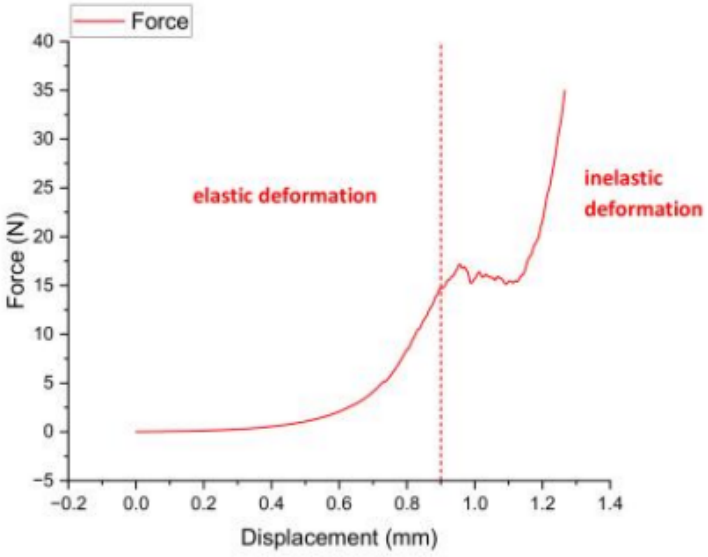

Figure 4. The compressive force-displacement curve of 3D printed skin and the elastic/inelastic deformation stage

DOI: 10.54254/2755-2721/2025.AST27297

Uniaxial compression tests quantified key parameters (elastic modulus, yield strength, fracture toughness) for tissue engineering applications.Linear force-displacement relationship during 0–0.8 mm displacement confirmed physiological stability, with elastic modulus calculated via slope ($E=\Delta F/\Delta\delta$).Beyond 0.8 mm displacement, irreversible deformation occurred, peaking at 34.98 N force and 0.29 MPa compressive stress [17].

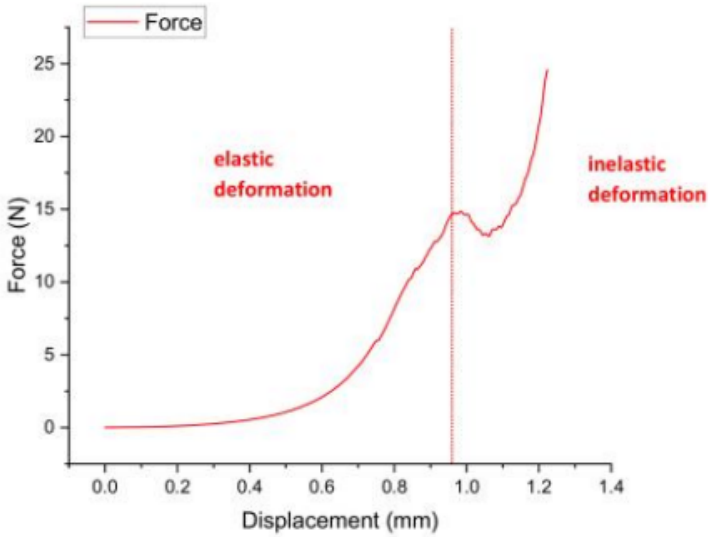

Figure 5. Schematic diagram of the force-displacement curve and deformation stage of material tensile

Uniaxial compression testing with force-displacement curve analysis quantified key parameters (elastic modulus, yield strength, fracture toughness) for tissue engineering applications like wound dressings and skin grafts.A linear force-displacement relationship occurred during initial low-strain deformation, confirming natural skin-like elastic modulus via slope calculation ($E=\Delta F/\Delta\delta$).Beyond critical displacement, the construct entered distinct plastic deformation, peaking at 24.57 N force and 0.2 MPa compressive stress [18].

DOI: 10.54254/2755-2721/2025.AST27297

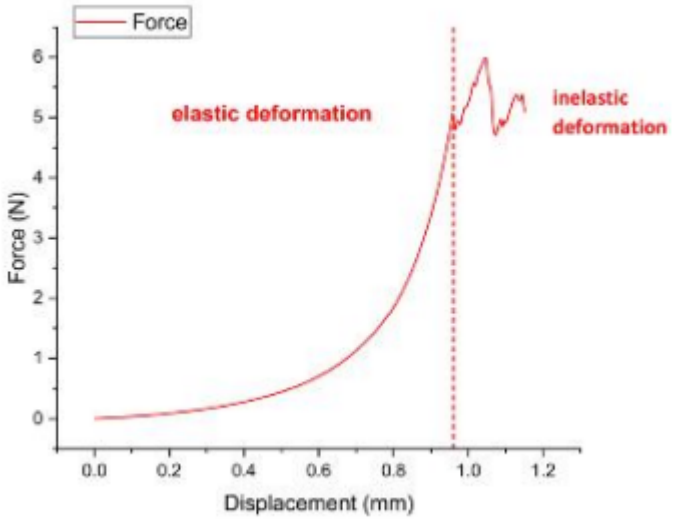

Figure 6. The force-displacement curve of the material tensile test and the schematic diagram of the elastoplastic deformation stage

Uniaxial compression testing revealed 3D-printed skin exhibits physiological-grade elastic recovery, demonstrated by a linear force-displacement relationship in the elastic phase. The calculated modulus (via slope $E=\Delta F/\Delta\delta$) confirms natural skin-like recoverability under load. Beyond critical displacement, the construct entered irreversible deformation with peak metrics of 5.99 N force and 0.05 MPa compressive stress – significantly below natural tissue benchmarks (0.1-0.2 MPa).

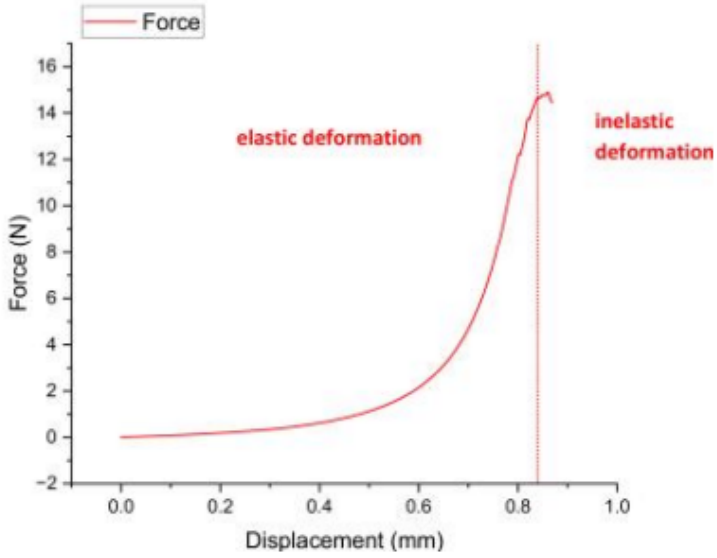

Figure 7. Testing of tensile mechanical properties of materials: force-displacement curves and characterization of elastoplastic deformation stages

Uniaxial compression testing revealed a linear force-displacement relationship during the elastic phase (0–0.6 mm displacement), enabling elastic modulus calculation via slope ($E=\Delta F/\Delta\delta$). Beyond 0.6 mm displacement, the material entered plastic deformation with a peak force of 14.9 N (0.12 MPa compressive stress) – aligning with natural skin ranges (0.1–0.2 MPa). However, irreversible

DOI: 10.54254/2755-2721/2025.AST27297

deformation in this phase necessitates fracture toughness enhancement for durable wound dressing/skin graft applications [19].

3.5. Evaluation of biomechanical properties of mouse skin

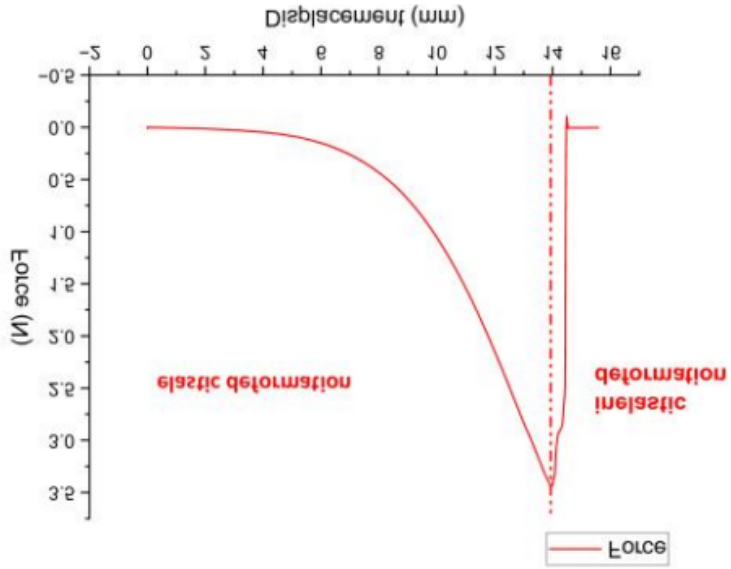

Figure 8. Tensile mechanical behavior of materials: force-displacement full curve and failure process schematic diagram

Uniaxial tensile testing of murine skin revealed a linear force-displacement relationship during elastic deformation (0-4mm displacement), enabling elastic modulus calculation via slope ($E=\Delta F/\Delta\delta$). These results demonstrate significantly higher rigidity than conventional 3D-printed skin substitutes (elastic modulus exceeding literature-reported 0.1-0.2 MPa ranges), suggesting enhanced physiological stability [20].

DOI: 10.54254/2755-2721/2025.AST27297

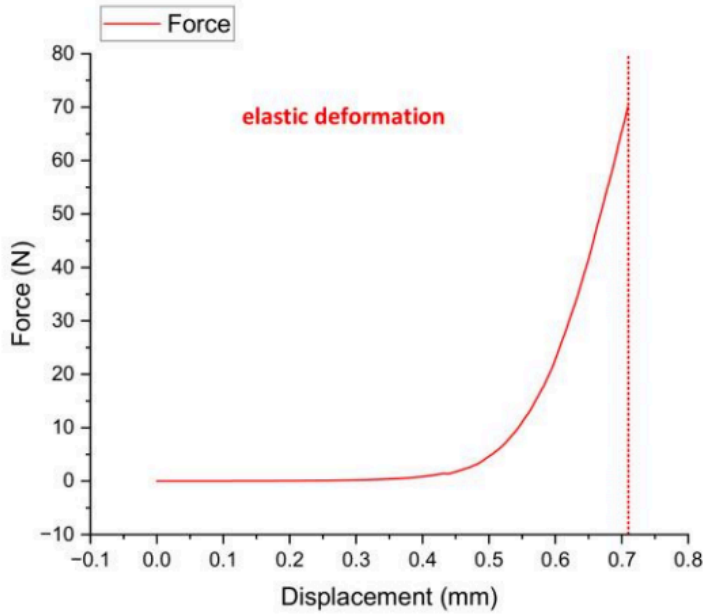

Figure 9. Force-displacement (F-D) curve of the material: schematic diagram of the elastic deformation stage

To analyze the compressive mechanical properties of experimental mouse skin and guide the design optimization of biomaterials (e.g., skin substitutes), this study conducted uniaxial compression tests with force-displacement curve analysis to measure key parameters including elastic modulus, yield strength, and fracture toughness. Results demonstrated a linear force-displacement relationship during the elastic deformation phase (0-approximately 0.3 mm displacement), with elastic modulus calculated via slope (formula: $E=\Delta F/\Delta\delta E=\Delta F/\Delta\delta$). Beyond approximately 0.3 mm displacement, the material entered the inelastic deformation phase, reaching a maximum force of 70.01 N and a maximum compressive stress of 0.7 MPa. These findings indicate that mouse skin exhibits high rigidity (elastic modulus significantly exceeding literature-reported values for 3D-printed skin) and compressive stress near the upper limit of natural skin (0.5-0.8 MPa). However, rapid failure in the plastic phase suggests insufficient fracture toughness, necessitating structural optimization to enhance damage resistance. Complementary biocompatibility testing is critical to ensure clinical applicability, providing essential biomechanical benchmarks for bioinspired skin development.

4. Discussion

The compressive Young's modulus of the bioprinted construct (193.09 kPa) aligns with human dermal values (50–500 kPa), confirming that the 5% GelMA/1% HAMA formulation achieves biomechanical relevance for skin simulation. GelMA provides structural integrity through photopolymerization-driven crosslinking, while HAMA enhances deformation resistance via additional covalent bonds. Crucially, this bioink composition directly dictates mechanical behavior —higher polymer concentrations would increase stiffness at the cost of nutrient diffusion. The photopolymerization process enables precise spatial control of crosslinking density, permitting future designs to mimic native tissue stiffness gradients. However, the embedded 500 μm vascular channel (occupying >19.5% cross-sectional area) introduces intentional structural heterogeneity,

DOI: 10.54254/2755-2721/2025.AST27297

redistributing stress concentrations during compression and reducing overall stiffness compared to solid hydrogels. While photopolymerization ensures accurate channel positioning without delamination, the current straight-channel design cannot replicate the mechanical reinforcement of branched microvasculature in native dermis.

Murine skin compression data revealed significant artifacts: An extended toe region (persisting to ~40% strain) with minimal force development (<1 N) indicated delayed collagen fiber engagement, likely due to hydration/mounting effects. Force accumulation only beyond 40% strain (reaching 50 N at 70% strain) contradicted preconditioned murine studies where collagen recruitment typically initiates at 20% strain. The calculated modulus (986.3 kPa) represents an artifact—derived from the steep terminal curve segment rather than physiologically relevant strains—and contradicts established preconditioned values at functional strains (<20%). This discrepancy stems from absent preconditioning cycles, where the initial 40% strain acted as uncontrolled preconditioning, invalidating direct comparison to the bioprinted hydrogel's quasi-linear response. Similarly, the murine tensile modulus (2.46 kPa) was three orders lower than its compressive measurement yet inconsistent with literature, further highlighting methodological constraints in cross-test comparisons.

5. Conclusion

While the photopolymerization-fabricated vascularized skin construct demonstrated human-relevant compressive properties (193.09 kPa modulus), attributable to its optimized 5% GelMA/1% HAMA hydrogel matrix and mechanical discontinuity from embedded 500 μm vascular channels, direct comparison with murine skin data proved invalid due to methodological limitations. The murine compressive modulus (986.3 kPa) represented only the non-physiological toe region of its stress-strain curve, failing to capture functional biomechanics. Future work must implement tissue preconditioning protocols, develop branched vascular architectures to better replicate native mechanobiology, and utilize tunable photopolymerization parameters to establish hierarchical mechanical emulation of human skin. Comprehensive validation thus requires overcoming these limitations through targeted investigation of crosslink density gradients, long-term matrix remodeling, and enhanced strain thresholds.

1:https://www.sciencedirect.com/science/article/abs/pii/S014296121500719X?via%3Dihub

2:https://www.nature.com/articles/nprot.2016.037

3:https://onlinelibrary.wiley.com/doi/10.1111/wrr.12402

References

[1] F P , R S , J P , et al. Concordance of in vivo reflectance confocal microscopy and horizontal-sectioning histology in skin tumours. [J].Journal of the European Academy of Dermatology and Venereology : JEADV, 2023, 38(1): 124-135.

[2] Bo C P , Bjørn L S , Børsen M R . Non-melanoma skin cancer excision with frozen section histology. [J].Danish medical journal, 2023, 70(5):

[3] Boaz A , Eli S , Evgenia V , et al. Alleviation of Severe Skin Insults Following High-Dose Irradiation with Isolated Human Fetal Placental Stromal Cells [J].International Journal of Molecular Sciences, 2022, 23(21): 13321-13321.

[4] Stéphane B , Valérie U , Taha H M , et al. Label-Free Infrared Spectral Histology of Skin Tissue Part II: Impact of a Lumican-Derived Peptide on Melanoma Growth. [J].Frontiers in cell and developmental biology, 2020, 8377.

[5] Histology - Molecular Histology; Data from Shanghai Jiao Tong University School of Medicine Provide New Insights into Molecular Histology (GelMA combined with sustained release of HUVECs derived exosomes for promoting cutaneous wound healing and facilitating skin regeneration) [J].Chemicals & amp; Chemistry, 2020,

DOI: 10.54254/2755-2721/2025.AST27297

[6] Clinical findings, histology, and management of nonmelanoma skin cancer in cancer survivors previously treated with radiotherapy [J].Journal of the American Academy of Dermatology, 2018, 79(3): AB78-AB78.
[7] Intracellular Signaling Peptides and Proteins - Phosphoinositide Phospholipase C; Findings from Sun Yat Sen University in the Area of Phosphoinositide Phospholipase C Described (Abnormalities of hair structure and skin histology derived from CRISPR/Cas9-based knockout of phospholipase C-delta 1 in mice) [J].Journal of Engineering, 2018, 2696-.
[8] Breuninger H , Belova A I . Microscopically controlled surgery with threedimensional histology tumescent local anesthesia and intracutaneous sutures for high tension in the treatment of skin cancer [J].Opuholi Golovy i Šei, 2018, 8(3): 21-36.
[9] A E T . The histology of skin treated with a picosecond alexandrite laser and a fractional lens array. [J].Lasers in surgery and medicine, 2016, 48(7): 646-52.
[10] Arif C , Michael S , Branko B , et al. Defining the Role of Skin and Mucosal Biopsy in Facial Allotransplantation: A 2-Year Review and Analysis of Histology. [J].Plastic and reconstructive surgery, 2015, 136(3): 559-67.
[11] Vaudrey C . Histology of Skin Lesion [J].Endocrinology & amp; Metabolic Syndrome, 2015, 4(3): 1-1.
[12] Jin W S , Jun H C , Man Y L , et al. Clinical analysis of an ultrasound system in the evaluation of skin cancers: correlation with histology. [J].Annals of plastic surgery, 2014, 73(4): 427-33.
[13] Anonymous . Non-Melanoma Skin Cancer Histology; Data from P. Thomson et al provide new insights into non-melanoma skin cancer histology [J].Biotech Week, 2010,
[14] L S C M , Jörg R . Histology of melanoma and nonmelanoma skin cancer. [J].Advances in experimental medicine and biology, 2008, 624215-26.
[15] Ross R , DiGiovanna J J , Capaldi L , et al. Histopathologic characterization of epidermolytic hyperkeratosis: A systematic review of histology from the National Registry for Ichthyosis and Related Skin Disorders [J].Journal of the American Academy of Dermatology, 2008, 59(1): 86-90.
[16] Bhattacharyya K T , Linton J , Mei L , et al. R402 – Profilometry and Skin Histology with Anti-wrinkle Agents [J].Otolaryngology - Head and Neck Surgery, 2008, 139(2S1): P177-P178.
[17] L A M , R A I , E D B , et al. Histology of ferret skin: preweaning to adulthood. [J].Veterinary dermatology, 2007, 18(6): 401-11.
[18] A I M , A C M D , Heliomar V A D , et al. Histology of the sternal and suprapubic skin areas in lion tamarins (Leontopithecus sp. Callitrichidae-primates). [J].American journal of primatology, 2006, 68(11): 1120-6.
[19] R P C , E K S , R B N . Basal cell carcinoma with mixed histology: a possible pathogenesis for recurrent skin cancer. [J].Dermatologic surgery : official publication for American Society for Dermatologic Surgery [et al.], 2006, 32(4): 542-51.
[20] Z A D , Lesniewski- K K , Joseph K , et al. Skin rash and bronchoalveolar histology correlates with clinical benefit in patients treated with gefitinib as a therapy for previously treated advanced or metastatic non-small cell lung cancer. [J].Lung cancer (Amsterdam, Netherlands), 2006, 51(1): 89-96.